Journal of Energy Storage 125 (2025) 116831

Contents lists available at ScienceDirect

Journal of Energy Storage

journal homepage: www.elsevier.com/locate/est

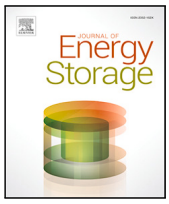

Research papers

Polyaromatic hydrocarbons as prospective anode materials for metal ion battery

Ilya V. Chepkasov [a,b,*], Viktor S. Baidyshev [a], Alexander G. Kvashnin [a]

[a] Skolkovo Institute of Science and Technology, Bolshoy Boulevard 30, bld. 1, Moscow 121205, Russian Federation
[b] Katanov Khakas State University, 90 Lenin pr., 655017, Abakan, Russian Federation

ARTICLE INFO

Keywords:
Polyaromatic hydrocarbons
Ion battery
Intercalation
Metal ions
Anode materials
First-principles calculations

ABSTRACT

Carbon-based compounds are promising anode materials for secondary metal-ion batteries due to their high capacity, low operating voltage, and high electronic conductivity of intercalated alkali and alkaline earth metal atoms. Bulk crystals of polyaromatic hydrocarbons (PAHs) of naphthalene, anthracene, tetracene and pentacene intercalated with alkali and alkaline earth metal atoms (Mg, Ca, Li, Na, K, Rb) are considered here as promising candidates for applications as anode materials using first-principles calculations. It is found that intercalation of Ca, Li, Na atoms in the pentacene crystal leads to the smallest volume change (5.2%, 0.8%, 3.4% respectively), indicating that pentacene structures can be used for batteries. The capacity of PAH crystals with Li, Na, K and Rb can be ~ 1.2–1.3 times higher than the theoretical capacity of lithium intercalated graphite, while the intercalation of Mg and Ca leads to even higher capacities, which are ~ 2.3–2.6 times higher. Our results provide important fundamental and practical information on the prospects of using the intercalated polyaromatic hydrocarbon crystals for energy storage applications due to their high theoretical capacity.

1. Introduction

The advent and evolution of lithium-ion batteries has transformed every facet of human existence. This scientific and technological breakthrough was duly recognized in 2019 when the Nobel Prize in Chemistry was awarded to Goodenough, Whittingham and Yoshino for their contributions to the development of lithium-ion batteries. Lithium-ion batteries are now one of the most important renewable energy sources due to their high gravimetric and volumetric energy density, high specific power, long life and low self-discharge [1–12]. They are also the most efficient secondary energy source for portable and mobile devices and are widely used in electric transport [13].

Global demand for lithium-ion batteries is expected to grow significantly over the next decade. Demand is expected to grow from around 700 GWh in 2022 to around 4.7 TWh in 2030. The vast majority of this demand will be for batteries used in mobility applications, such as electric vehicles, which are expected to account for around 4300 GWh in 2030 [14]. Such high demand for lithium-ion batteries is leading to a dramatic increase in the price of metallic lithium. There is therefore an urgent need to develop batteries with cheaper metal cations as mobile ions and also to develop new types of batteries with higher gravimetric or volumetric energy density. In this regard, increasingly batteries based on sodium (Na) [15,16], potassium (K) [17,18], rubidium (Rb) [19], magnesium (Mg) [20,21], and calcium (Ca) [22,23] due to the high abundance of these elements on Earth and therefore their potentially lower overall cost compared to lithium.

To meet the ever-increasing demand for high capacity and energy density, considerable efforts have been made to search for new anode materials with high capacity [24–33]. Among them, carbon-based materials have attracted much attention because they can reversibly absorb and release lithium ions at low electrochemical potential. Currently, synthetic graphite materials dominate as anodes for lithium-ion batteries, due to their good specific capacity and cycle life [29,34]. However, the production of synthetic graphite requires a high-temperature graphitization process at temperatures above 2500 °C, which results in higher processing costs. One of the directions in the search for new anode materials for metal-ion batteries is the study of organic materials as environmentally friendly and high performance anode materials. Switching from inorganic to organic anode materials, which are widely available on earth, is more cost effective and has several distinct advantages in ion batteries. They are not dependent on critical materials as they can be synthesized from readily available natural sources and biomass. In addition, organic materials have known adaptable structural designs and are less hazardous than conventional anode materials [35–37]. A key advantage of organic anode materials is their structural flexibility, which improves their overall electrochemical

* Corresponding author at: Skolkovo Institute of Science and Technology, Bolshoy Boulevard 30, bld. 1, Moscow 121205, Russian Federation.
E-mail address: I.Chepkasov@skoltech.ru (I.V. Chepkasov).

https://doi.org/10.1016/j.est.2025.116831
Received 7 January 2025; Received in revised form 7 April 2025; Accepted 27 April 2025

performance, making organic anode materials a promising alternative for next-generation ion batteries [38].

In particular, polycyclic aromatic hydrocarbon (PAH) molecules, such as benzene, naphthalene, anthracene and tetracene, have been the subject of considerable research as potential materials for high-capacity batteries [39–50]. PAHs have emerged as a promising material for batteries due to their redox activity and the availability of intercalation sites, which is a consequence of their unique arrangement of molecules within the crystal lattice. In particular, the molecules within PAH crystals are held together by van der Waals dispersion forces, and the crystals are flexible enough to allow the insertion of intercalants. In addition, these materials are malleable, inexpensive, environmentally benign, and widely accessible [51–54]. PAH systems have been considered as prototypical carbonaceous materials, mimicking sp^2 allotropic forms of carbon, and also as organic solids capable of storing sufficiently large amounts of energy to be of practical use. The adsorption of lithium atoms onto polyaromatic hydrocarbons demonstrated the potential of these materials for use in lithium-ion batteries [55–58]. In a study using semi-quantitative methods, Friedlein et al. [59] compared the charge storage capacity of PAHs and showed that small and medium-sized PAHs may have the highest energy storage capacity of all pure carbon systems. Arya et al. [60], showed that small molecule polycyclic aromatic hydrocarbons such as naphthalene, biphenyl, 9,9-dimethylfluorene, phenanthrene and p-terphenyl are promising anode materials for lithium-ion batteries with impressive cycle stability, high specific capacity and excellent rate capability.

However, despite the prospects of PAHs as anode materials, the intercalation of alkali and alkaline earth metal atoms into PAH crystals has not yet been systematically studied in the context of energy storage with a detailed comparison of different metal ions and PAHs to select a prospective anode material for metal ion batteries. In order to evaluate the prospects of PAHs as anode materials for metal-ion batteries, the intercalation of Li, Na, K, Rb, Mg, Ca into PAH crystals such as naphthalene (NP), anthracene (AN), tetracene (TN) and pentacene (PN) has been systematically studied using density functional calculations.

2. Methods

The calculations were performed using the density functional theory as implemented in the VASP software package [61–63]. The exchange–correlation functional was used in the Perdew–Burke–Ernzerhof parametrization (PBE) [64]. The plane-wave energy cutoff was set to 600 eV. The Monkhorst–Pack grid points [65] 4 × 4 × 4 and 12×12×12 were used to sample the first Brillouin zone of the considered primitive cells of PAH crystals and metals respectively. Relaxation of simulated structures was carried out until the total energy difference and the atomic net forces become less than 10^{-5} eV and 10^{-4} eV /Å, respectively, to ensure high accuracy and convergence of the calculations. The atomic structures and the charge densities were illustrated using the VESTA package [66]. The diffusion barriers for metal atoms in the PAH crystals were examined using the climbing image nudged elastic band (CI-NEB) [67] approach with 14 images constructed for each diffusion pathway.

To study the energetics related to the intercalation and relative stability of the considered structures with alkali and alkaline earth metal (M = Li, Na, K, Rb, Mg, Ca), the intercalation energy per metal atom, E_i, which defines the change in energy when n_M metal atoms are moved from the corresponding bulk into the PAH, was calculated and can be evaluated as follows:

$$E_i = \frac{E(n_M) - E(0)}{n_M} - \mu_M, \tag{1}$$

where $E(n_M)$ is the total energy of the intercalated PAH crystal, $E(0)$ is the energy of the original PAH crystal, and μ_M is the chemical potential of the atom in the bulk structure. Negative values indicate that intercalation is more favorable for a particular metal atom than being in an infinite metal crystal.

The thermodynamic phase stability of the systems was also assessed using phase diagrams in (enthalpy of formation - composition) coordinates (convex hulls). From the DFT energies of pseudo-binary phase M_xPAH_{1-x} with M and PAH blocks the enthalpy of formation per block is calculated:

$$E_f/block = E(M_xPAH_{1-x}) - xE(M) - (1-x)E(PAH), \tag{2}$$

where $E(M_xPAH_{1-x})$ is the total energy of M-intercalated polyacene system.

A convex hull was constructed between the points (x, $E_f/block$) = (0, 0);(1,0). Lines connect structures with the lowest energy, so that they form a convex hull. Structures on the convex hull are thermodynamically stable, and structures above the convex hull are metastable (their decomposition energies are positive).

The concentration x of metal atoms in PAH is defined as follows:

$$x = \frac{n(M)}{n(M) + n(PAH)}, \tag{3}$$

and the number of metal atoms n is the number of atoms per formula unit of the polyacene molecule (there are two molecules in the unit cell).

The theoretical capacity of the PAH crystals with metal atoms was calculated using the Faraday's law:

$$Capacity = \frac{\nu \cdot z \cdot F}{3.6 \cdot M} \tag{4}$$

where ν is the number of metal atoms per polyacene molecule, F is the Faraday constant, which is 96485 C/mol, M is the molar mass of the polyacene molecule, z is the formal charge of the metal ion.

For PAH crystals, the volume change (ΔV) is calculated using the following equation:

$$\Delta V = \frac{V_i - V_p}{V_p} \cdot 100\% \tag{5}$$

where V_i and V_p represent the volume of intercalated PAH crystal and pristine PAH crystal.

Average voltages for the thermodynamically stable structures were calculated from the DFT total energies. For two phases on a convex hull, M_{n_1}PAH and M_{n_2}PAH ($n_2 > n_1$), the following reaction is assumed to occur:

$$M_{n_1}PAH + (n_2 - n_1)M \rightarrow M_{n_2}PAH \tag{6}$$

The voltage, V, is calculated by the following formula:

$$V = -\frac{\Delta G}{z(n_2 - n_1)} \approx -\frac{\Delta E}{z(n_2 - n_1)} = -\frac{E(M_{n_2}PAH) - E(M_{n_1}PAH)}{z(n_2 - n_1)} + \frac{E(M)}{z} \tag{7}$$

where the Gibbs free energy is approximated by the internal energy, as pV and thermal energy assumed to be small, z = is a formal charge of metal ion, M — metal.

The Crystal Orbital Hamilton Population (COHP) method is used to investigate the chemical bonding between metal atoms and the PAH crystals. In order to extract information about chemical bonding from the electronic density of states (DOS) of a crystal, the crystal orbital overlap population (COOP) was calculated.

COOPs are obtained by multiplying the DOS by the number of overlaps (population). This allows the total electron density to be separated into bonding and anti-bonding states. Consequently, the theory of crystal orbital Hamilton populations (COHP) has been proposed, which generates populations of overlapping orbitals. The sign of COHP is opposite to that of COOP in the case of bonding and anti-bonding states. Therefore –COHP diagrams are always constructed for clarity. The COHP provides a straightforward method of obtaining data on the bonding and anti-bonding states. The mathematical representation of the COHP bears a striking resemblance to a projected DOS equation, but with the density of state matrix weighted by the Hamiltonian matrix

elements. In the case of periodic crystals, the COHP can be defined as follows [68]:

$$COHP_{AB}(\epsilon) = \sum_{\nu \in A} \sum_{\mu \in B} COHP_{\mu\nu}(\epsilon) \tag{8}$$

$$COHP_{\mu\nu}(\epsilon) = \frac{2}{V_{BZ}} \int_{BZ} H_{\mu\nu}(k) \left\{ \sum_{j} c^{*}_{\mu j}(k) c_{\nu j}(k) \delta(\epsilon - \epsilon_{j}(k)) \right\} dk \tag{9}$$

where $H_{\mu\nu}(k)$ is the Hamiltonian matrix in reciprocal space, $c_{\mu j}(k)$ are the expansion coefficients of the jth occupied crystal orbital with the energy $\epsilon_j(k)$ in terms of Bloch functions numbered in the same way as atomic orbitals by the subscript μ or ν. Integration over k in the Eq. (9) is performed in the Brillouin zone (BZ) with the volume V_{BZ}.

The negative and positive COHP values, respectively indicating bonding and anti-bonding interactions, result from the weighting of the elements of the Hamiltonian matrix. Integration of COHP up to the Fermi level (E_F) gives integrated COHP (ICOHP) values.

$$ICOHP_{AB} = \int_{E_F} COHP_{AB}(\epsilon) d\epsilon \tag{10}$$

All COHP calculations were conducted using the LOBSTER algorithm [69], and further analysis of the contribution of each orbital to the total binding energy was performed using the Dragon software package.

Ionic conductivity (σ) in PAHs is calculated based on the diffusion barriers according to the following relation:

$$\sigma = n \cdot q \cdot D_0 \cdot e^{-\frac{E_a}{k_B T}} \tag{11}$$

where the pre-exponential factor D_0 is taken to be 10^{-9} m^2/s, which is the usual value for ionic diffusion in organic crystals, E_a is the activation energy, calculated using DFT, n is the number density of metal ions in the considered unit cell, q is the charge of the ions.

3. Results and discussion

Firstly, a preliminary study was carried out of different methods for delineating the van der Waals (vdw) interaction on the intercalation energy. Previous research has shown that the application of different vdW corrections can lead to markedly different results [70–73].

The methods for calculating the vdW interaction can be divided into three categories: semiempirical models proposed by Grimme et al. [74–76], models based on atomic polarization modified by electron density [77–80], and full density functional approximations based on pairwise dispersion models using only the electron density [81,82].

Four of the eleven available methods (MBD@rsSCS/FI+ER [80], DFT-D3 [75], optB88-vdW [83], and DFT-dDsC [79]) provide higher accuracy compared to other methods. Previously [72,73], it was reported that the most accurate method for describing chemical and dispersion forces in two-dimensional materials and molecular crystals is SCAN+rVV10 [84]. However, a major challenge associated with SCAN+rVV10 is its computational performance.

Several vdW force calculation methods are used to evaluate the intercalation energy of a metal atom (Mg, Ca, Li, Na, K, Rb) into the pentacene crystal as listed in the Table 1. The chemical potential of the metal atoms in the bulk structures, the charge transfer according to Bader's analysis and the volume of the pentacene crystal with metal atoms inside were also calculated as shown in Supporting Information Table S1–S3. All methods gave almost the same charge transfer (see Table S3 in the Supporting Information), but the calculated intercalation energies E_i were quite different for the different methods. The intercalation energy of a Li atom in pentacene is positive according to the DFT-TS and DFT-TS/HI methods (see Table 1), which is caused by a twice lower μ_{Li} compared to other methods. Thus, these methods are not suitable for describing the intercalation of alkali metals as shown previously [88]. The most accurate methods such as vdW-DF [81] and optPBE-vdW [83] give correct values for the tetracene lattice parameters [48], but underestimate the energy of the bulk alkali metals [32], which affects the intercalation energy (see Table 1). At the same time, the computationally efficient zero damping DFT-D3 method [75] gives reasonable values for the lattice parameters and energy used later in this study.

A proper vdW correction allows us to study the interaction of metal atoms with isolated PAH molecules and PAH crystals. For all studied metal atoms the same adsorption positions on the PAH molecules were considered. The intercalation energy E_i for metal atoms on the PAH molecules is calculated. In this case, the intercalation energy is the adsorption energy calculated using the energy of the bulk metal as a reference by Eq. (1). The dependence of E_i on the type of adsorbed metal atoms (Mg, Ca Li, Na, K and Rb) for four types of isolated PAH molecules, namely naphthalene (NP), anthracene (AN), tetracene (TN) and pentacene (PN) is shown in Fig. 1(a). It can clearly be seen that E_i decreases as the number of benzene rings in the PAH molecule increases, and that E_i is lowest for the pentacene molecule. The decrease in electronegativity from magnesium to rubidium according to Ref. [89], leads to a decrease in E_i. In the case of lithium, however, this general tendency is not observed. Such behavior for alkali metal atoms intercalated in a bilayer of graphene and graphite has been discussed previously [30,90,91]. This effect is due to a strong covalent bond between Li and carbon atoms [92] and the ionic contribution to the bond.

To illustrate this point, the difference between the electron charge densities of the combined and separated systems has been visualized on an isolated molecule of pentacene, as shown in Fig. 1(c). It is evident that the localization of the charge density on the covalent bonds between Li atom and the pentacene molecule is stronger (higher electron density concentration) compared to other metals, see Fig. 1(c).

The intercalation of a metal atom into PAH crystals is then studied by calculating the intercalation energy E_i using Eq. (1). Similar to isolated PAH molecules, the intercalation energy in PAH crystals decreases with increasing number of benzene rings, see Fig. 1(b). In contrast to isolated molecules, the largest deviation in intercalation energy in crystals is not for lithium but for calcium. This is due to the fact that under conditions of limited intermolecular space in the crystal, the large Coulomb interaction caused by the divalent charge becomes more pronounced. As in the case of isolated molecules the charge difference between the electron densities of the combined and separated systems has been visualized in the pentacene crystal, as shown in Fig. 1(d).

Analysis of the electron density redistribution for alkali metals shows that in the case of lithium there is a large charge redistribution on the bonds, as shown previously [30,90,91]. For alkaline earth metals (Mg and Ca), a stronger redistribution of electron density is observed compared to the case of isolated molecules due to the divalent charge and stronger Coulomb interaction. This is because the metal atom in the crystal interacts with three PAH molecules simultaneously (see Fig. 1(d)).

The Bader charge analysis method [93] is used to analyze the charge transfer from metal atoms to the PAH molecule or crystal. In the case of PAH crystals, alkali metal atoms (Li, Na, K, Rb) lose about 0.82–0.87 electrons for all PAH crystals considered (NP, AN, TN, PN). For the alkaline earth metals, the difference in atom type is more pronounced. In particular, the Ca atom loses about 1.42–1.46 electrons, whereas the Mg atom loses about 1.54–1.59 electrons. The dependence of the charge transfer from alkali metal atoms on the isolated PAH molecule on the atom type almost repeats the tendency for PAH crystals. This is because atoms are freer on isolated PAH molecules and the distance between molecules can be greater than in PAH crystals.

In order to study the chemical bonding of an intercalated/adsorbed metal atom on the PAH crystals or isolated PAH molecules in more detail, calculations of crystal orbital Hamilton populations (COHPs) are carried out as shown in Fig. 2(b). COHP provides the information

Table 1
Intercalation energy (E_i) of a one metal atom in a pentacene crystal calculated using different van der Waals corrections.

Method	$E_{i(Mg)}$, eV	$E_{i(Ca)}$, eV	$E_{i(Li)}$, eV	$E_{i(Na)}$, eV	$E_{i(K)}$, eV	$E_{(Rb)}$, eV
dDsC [79]	0.32	−1.16	−0.64	−0.39	−0.51	−0.51
DFT-D2 [74]	0.34	−1.52	−1.15	−0.89	−1.05	−1.17
DFT-D3 [75]	0.51	−1.09	−0.48	−0.31	−0.62	−0.71
DFT-D3-BJ [76]	0.51	−1.11	−0.47	−0.33	−0.57	−0.60
TS [78]	0.38	−1.11	1.05	0.45	1.86	1.98
TS/HI [85]	0.54	−0.89	1.48	0.87	2.28	2.39
optB86b-vdW [82]	0.19	−2.64	−0.67	−0.52	−0.75	−0.59
optB88-vdW [83]	0.21	−1.36	−0.68	−0.52	−0.73	−0.56
optPBE-vdW [83]	0.39	−2.54	−0.57	−0.45	−0.73	−0.58
rev-vdW-DF2 [86]	0.22	−2.62	−0.68	−0.51	−0.77	−0.64
SCAN-rVV10 [84]	0.07	−1.29	−0.94	−0.58	−0.20	−0.09
dW-DF [81]	0.58	−2.46	−0.45	−0.38	−0.75	−0.62
vdW-DF2 [87]	0.54	−2.35	−0.54	−0.37	−0.67	−0.54

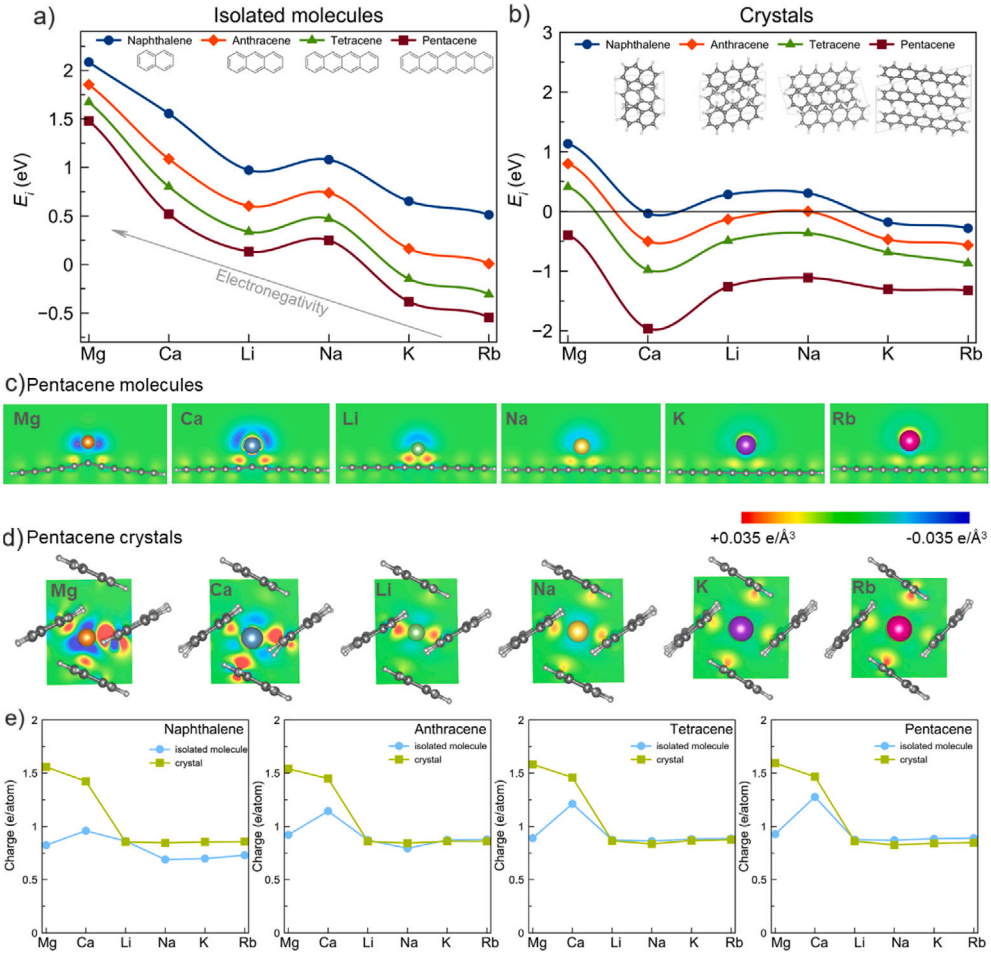

Fig. 1. (a) Energy required to remove a metal atom from the bulk crystal and adsorb it onto an isolated PAH molecule. (b) Calculated intercalation energy of a metal atom into PAH crystals. Visualization of charge transfer between metal atoms and (c) isolated pentacene molecule, (d) pentacene crystal. Red areas correspond electron density excess, blue areas to electron density deficiency. (e) Charge transfer from metal atoms to PAH crystals/isolated molecule depending on the type of metal atom. Blue line shows data for isolated molecules, green line for crystals. (For interpretation of the references to color in this figure legend, the reader is referred to the web version of this article.)

about the bonding and anti-bonding states in a simple way. The COHP analysis shows that there are more bonding states in the case of Mg and Ca (Fig. 2(b)). To estimate the strength of the chemical bond, the integrated COHP (ICOHP) is calculated. A more negative value of this indicates a stronger bond (Fig. 2(a)). As can be seen from the ICOHP analysis for the alkali metals, the bond strengths are approximately the same, varying from −0.24 to −0.17 eV/bond for pentacene crystal and from −0.18 to −0.11 eV/bond for the isolated pentacene molecule, see Fig. 2(a). However, for Mg and Ca the bonding becomes much stronger and the ICOHP is −1.57 and −1.28 eV/bond for Mg and Ca respectively in the case of the pentacene crystal and −0.74 and −0.63 eV/bond in the case of the isolated pentacene molecule. These results suggests that the stronger bonding of Mg atoms with PAH may lead to difficulties in the reversibility of the insertion/extraction process, especially at relatively high charge/discharge rates as has been shown in other host materials for Mg batteries [94,95].

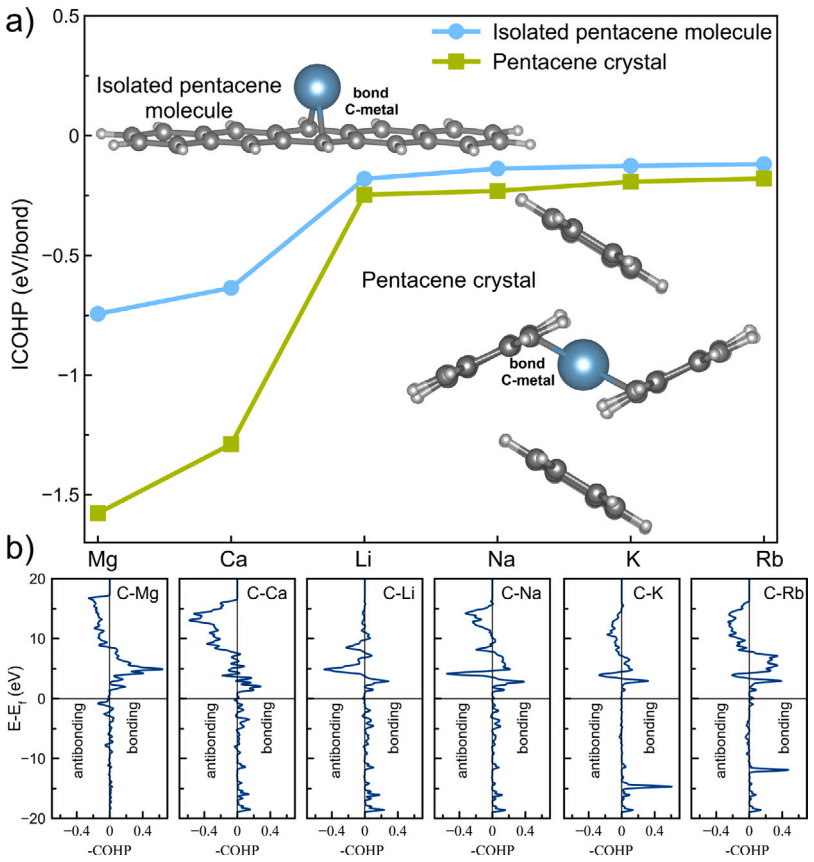

Fig. 2. (a) The integrated COHP (ICOHP) calculated for the metal-carbon bond in the case of the pentacene molecule and crystal. (b) COHP diagrams for the interaction between the metal atom and the nearest carbon atoms.

The intercalation of the maximum possible number of metal atoms into PAH crystals is then calculated to determine the intercalation energy, capacity and volume change of the studied PAHs. The maximum number of metal atoms intercalated in the crystal is calculated from the ratio of 1 metal atom per benzene ring in the PAH unit cell. It has previously been shown [30,48] that this concentration of intercalated metal atoms is optimal and does not lead to aggregation of metal atoms into clusters within the crystal with a corresponding significant increase in the volume of the structure. Consequently, PAH crystals with intercalated metal atoms in number $x = 4, 6, 8, 10$ for NP, AN, TN, PN are considered. Crystal structures of intercalated PAH crystals are shown in Fig. 3(a). The intercalation energy E_i calculated by Eq. (1) is shown in Fig. 3(b). A negative value of E_i means that the intercalation is energetically favorable. In the case of Mg, intercalation into PAH crystals is energetically unfavorable and such structures will not be stable. For the other considered types of metal atoms, the intercalation energy is negative and intercalation of these atoms in PAH crystals is most likely to occur. The only exception is the intercalation of Na into a naphthalene crystal, where the intercalation energy is slightly above zero, equal to 0.13 eV. However, phonon calculations have shown that only structures of tetracene and pentacene with Ca, Li, Na, K have no imaginary frequencies in the phonon spectra (see Figures S3–S10 in the Supporting Information). We have also calculated the products of the electrochemical reaction of considered PAHs with the alkali metal. Potential reactions are presented in Table S4 in the Supporting Information. The dynamical stability of these structures gives the possibility to obtain them experimentally with such concentrations of atoms. For these stable structures electronic density of states (Figures S11, S12 in the Supporting Information) have been calculated. Moreover, *ab initio* molecular dynamics calculations are performed at 900 K for 5 ps (with the timestep of 1 ps) to indicate thermal stability of studied compounds (see Figures S13–S16 in the Supporting Information). For these calculations, the $1 \times 2 \times 1$ supercells are used for the simulation. These data show the stability of the structures with respect to the high temperature oscillations of the atoms, allowing us to infer their stability.

An important factor in determining the applicability of a material as an anode material for metal-ion batteries is the magnitude of the volume change of the materials during ion intercalation. The large ionic radii of the K and Rb atoms are expected to result in the largest changes in PAH volume (see Fig. 3(c)). The smallest change in volume occurs when Ca, Li, Na atoms are intercalated in the pentacene crystal (5.2%, 0.8%, 3.4% for Ca, Li, Na respectively), which are important results indicating the possibility of using pentacene crystals with Ca, Li, Na in batteries. The correlation between $(C_{12} - C_{44})/B$ and the Pugh ratio for the structures of tetracene and pentacene with Ca, Li, Na, K with full concentration of metal atoms are calculated (see Figure S19 in the Supporting Information). As the concentration of intercalated metals increases, the whole material starts to behave like a more ductile material compared to pure PAH crystal.

The capacity of PAH crystals with different metal atoms and different concentrations was analyzed. The theoretical capacity was calculated using Faraday's law (Eq. (5)). The dependence of the capacity on the type of intercalated metal atoms for different PAH crystals compared to the theoretical capacity of lithium intercalated graphite (as the most popular anode material in ion batteries) is shown in Fig. 3(d), (e). In the case of alkali metals (Li, Na, K, Rb), the capacity of PAHs can be ~ 1.2–1.3 times greater than the theoretical capacity of lithium-intercalated graphite (dashed horizontal line in Fig. 3(d)). In the case of Mg and Ca atoms, the capacity of PAHs can be ~ 2.3–2.6

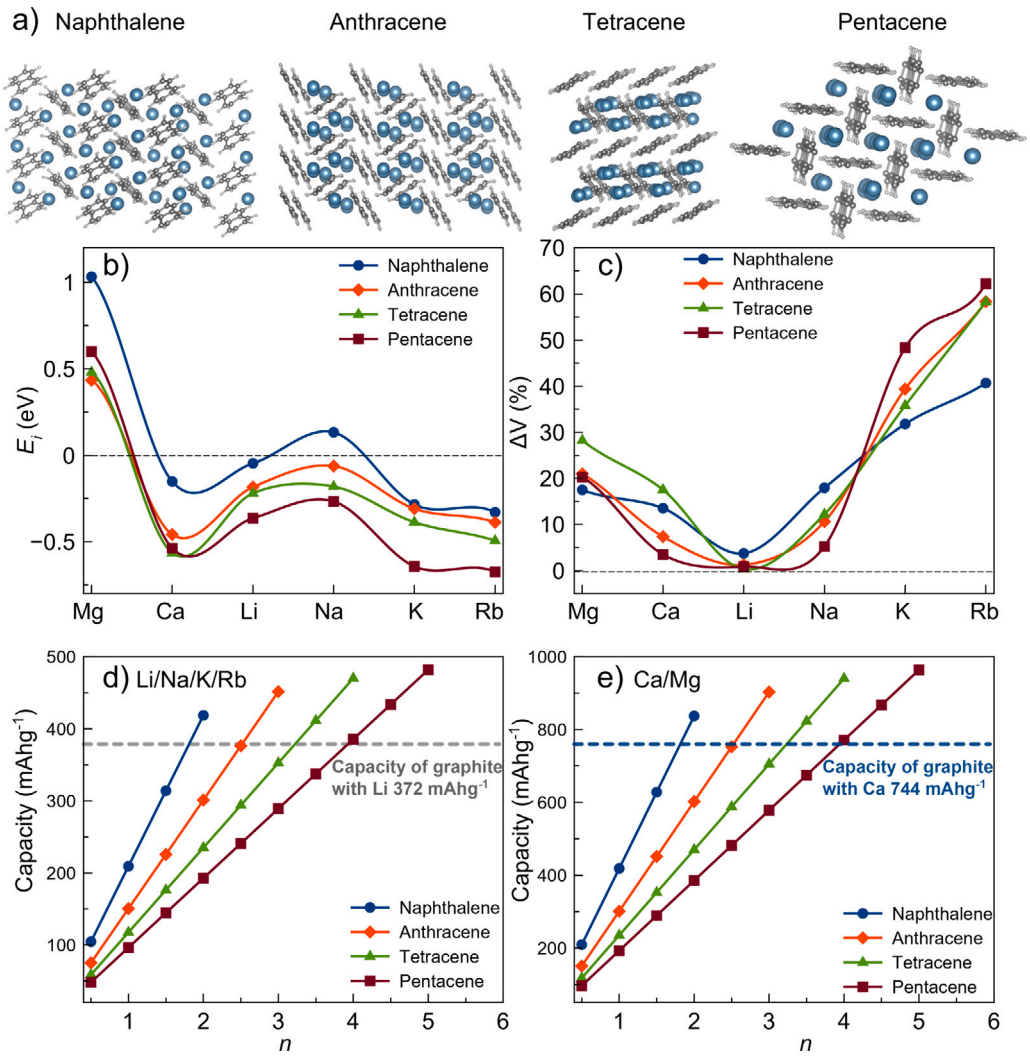

Fig. 3. (a) Crystal structures of naphthalene, anthracene, tetracene and pentacene crystals with intercalated metal atoms. The number of metal atoms per unit cell is 4, 6, 8, 10 for NP, AN, TN, PN respectively. (b) Intercalation energy as a function of the type of metal atoms. (c) Change in crystal volume as a function of the type of intercalating atom. (d,e) Calculated capacity of the intercalated PAH crystals.

times greater than that of lithium-intercalated graphite. The maximum capacity (418 mAhg^{-1},) we obtained for naphthalene with Li is close to the capacity obtained experimentally (435 mAhg^{-1}) in Arya et al. [60]. So, hypothetically, PAH crystals could be a more capacious anode material than graphite.

Also the phase diagrams in the coordinates of enthalpy of formation — composition (convex hull) for structures of tetracene and pentacene with Ca, Li, Na, K are calculated. Values of E_i for all calculated structures are negative, but not all structures lie on the convex hull, indicating that some structures may be metastable. The highest concentrations of metals at which the structures are thermodynamically stable are $x = 0.75$ ($n = 3$), $x = 0.66$ ($n = 2$), $x = 0.75$ ($n = 3$) and $x = 0.75$ ($n = 3$) for Li, Na, K and Ca in tetracene (Fig. 4(a)–(d)) and $x = 0.8$ ($n = 4$), $x = 0.66$ ($n = 2$), $x = 0.8$ ($n = 4$) and $x = 0.8$ ($n = 4$) for Li, Na, K and Ca in pentacene (Fig. 5(a)–(d)). Average voltages are calculated for the stable structures shown on the convex hull (Fig. 4(e)–(h) and Fig. 5(e)–(h)). Low Li, K, and Ca insertion voltages at high concentration indicate the possibility of high performance of PAH as anode materials.

Finally, to gain insight into the intercalation kinetics, the diffusion barriers for the intercalated atoms were calculated. The diffusivity of the intercalated atom is an important factor that can determine the actual operation of the ion battery, since the charge/discharge of metal-ion batteries depends mainly on the diffusion of metal atoms in the anode materials. Using the CI-NEB [67] approach the diffusion barriers for Mg, Ca Li, Na, K and Rb atoms in naphthalene, anthracene, tetracene and pentacene crystals were calculated as shown in Fig. 6. It was found that for different types of metal atoms different positions in the PAH crystals are most energetically favorable (Figure S1a in the Supporting Information). The most favorable position for Mg, Li and Ca atoms is between molecules in anthracene, tetracene and pentacene (position 1 in Figure S1b in the Supporting Information). On the other hand for K and Rb atoms, it is energetically more favorable to be between the stacked PAH molecules (position 2 in Figure S1b in the Supporting Information). It is to note interesting that in the case of Na, the energy difference between positions 1 and 2 is quite small for anthracene, tetracene and pentacene crystals (Figure S1a in the Supporting Information). This may be a key to understanding the low diffusion barrier for Na. For naphthalene, the most energetically favorable position for all considered atom types is the position between the stacked molecules (position 2 in Figure S1 in the Supporting Information). The reason for this is the size of the naphthalene molecules, which are short and consist of only two benzene rings (Figure S1b in the Supporting Information).

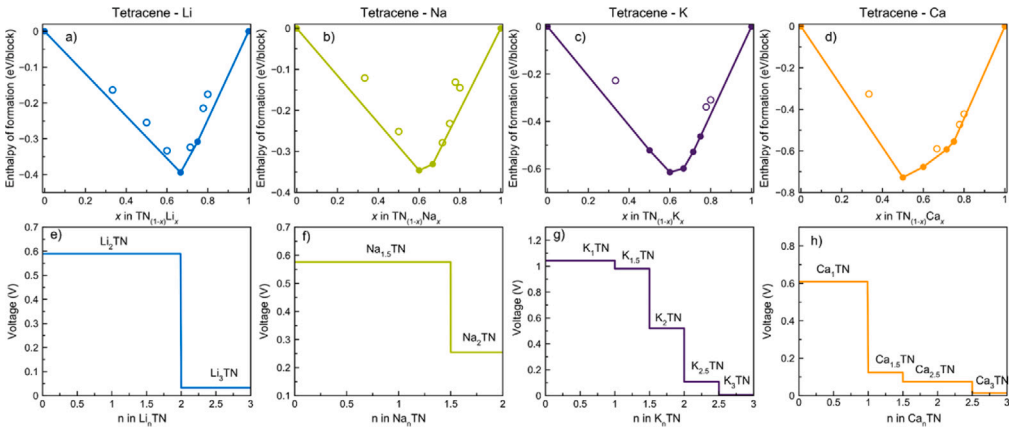

Fig. 4. Calculated convex hulls of the crystalline TN-Li (a), TN-Na (b), TN-K (c) and TN-Ca (d) systems with respect to pristine crystalline PAH and crystalline metal. Calculated average voltages relative to metal for TN-Li (e), TN-Na (f), TN-K (g) and TN-Ca (h) structures on the convex hull (a–d).

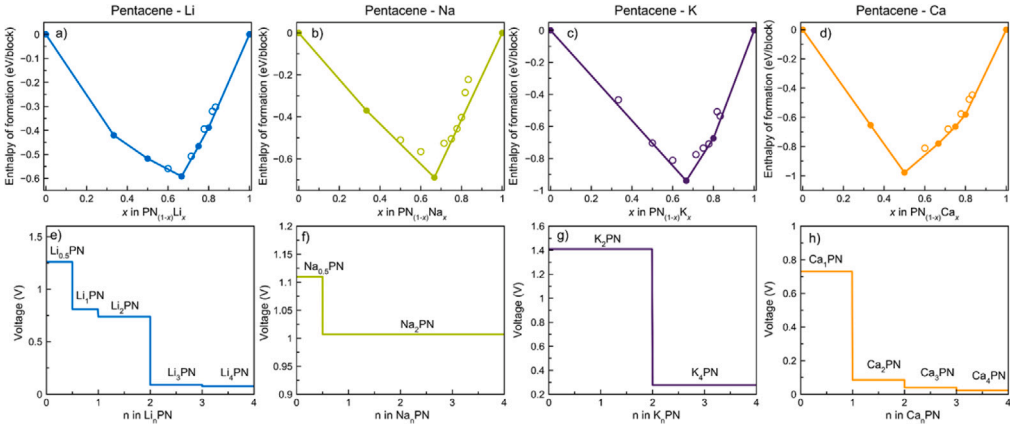

Fig. 5. Calculated convex hulls of the crystalline PN–Li (a), PN–Na (b), PN–K (c) and PN–Ca (d) systems with respect to pristine crystalline PAH and crystalline metal. Calculated average voltages relative to metal for PN–Li (e), PN–Na (f), PN–K (g) and PN–Ca (h) structures on the convex hull (a–d).

Taking this into account different diffusion pathways were considered for Mg, Ca, Li (path I, path II) and for Na, K, Rb (path III, path IV) as shown in Fig. 6 as insets. In the case of Mg, Ca, Li (path I, path II) diffusion is governed by the 'jumps' between molecules (Fig. 6(a)–(d)). For all considered PAH crystals the diffusion barriers for Li and Ca are relatively low and do not exceed 0.6 eV for Li and 0.95 for Ca. Taking into account diffusion along the molecule (path I), the values obtained for Li are in good agreement with those for bilayer graphene (BLG) (energy barrier for AA stacking is 0.34 eV, for AB stacking the barrier is 0.07 eV) [96]. Only diffusion along the naphthalene molecule is ~ 1 eV, which is quite high compared to other crystals.

The diffusion barriers obtained for sodium are of considerable interest. The energetic equivalence of the positions between the stacked molecules and between molecules for Na in anthracene, tetracene, and pentacene crystals implies that the 'jump' barrier between molecules will be insignificant, as previously demonstrated in tetracene crystals [48]. The diffusion barriers along the PAH molecule for Na in anthracene, tetracene, and pentacene are less than 0.3 eV, 0.45 eV, and 0.45 eV, respectively. This is lower than the diffusion barrier for Li in pentacene crystals. Given the relatively high diffusion barriers along Path III for Na, it can be anticipated that Na will diffuse along the molecule, with diffusion barriers comparable to or lower than those of Li. The diffusion barrier for Mg, K and Rb is higher compared to previous metals, which is due to the strong bonding with PAH molecules in the case of Mg and the large ionic radius in case of K and Rb atoms.

The diffusion barriers for Ca, Li, Na, K into tetracene and pentacene with highest possible concentration of metal atoms are calculated (see Figure S17 and S18 in the Supporting Information). The diffusion barrier for Li and Ca in tetracene with highest metal concentration compared to diffusion in an empty tetracene crystal increases from 0.58 to 0.85 eV for Li and from 0.92 to 1.13 eV for Ca. The same behavior is observed for Li and Ca in the pentacene, where the diffusion barrier increases from 0.62 to 0.81 eV for Li and from 0.79 to 1.43 eV for Ca. This is due to the fact that the intercalation of Li and Ca atoms does not lead to a large increase in the volume of PAH crystals (as shown in Fig. 3(c)). Thus, increase the concentration of metal atoms inside the PAH changes the diffusion in different ways. This is also shown by the ionic conductivity that is calculated based on the diffusion barriers (see Figure S20 in the Supporting Information). It is observed that for intercalation of sodium and potassium the ionic conductivity increases with increasing their concentration, while for the others the opposite situation is observed. This unobvious behavior is explained by the fact that during intercalation K, due to its large ionic radius, strongly increases the volume of the PAH crystal (as shown in Fig. 3(c)), which leads to the appearance of large diffusion channels inside the PAH crystal.

4. Conclusions

The energetics of intercalation and diffusion of metal atoms (Mg, Ca, Li, Na, K, Rb) in the polyaromatic hydrocarbon crystals, namely naphthalene, anthracene, tetracene and pentacene have been studied using DFT calculations. Calculations of intercalation energy and phonon spectra showed that tetracene and pentacene structures with Mg and Rb are not stable together with naphthalene and anthracene

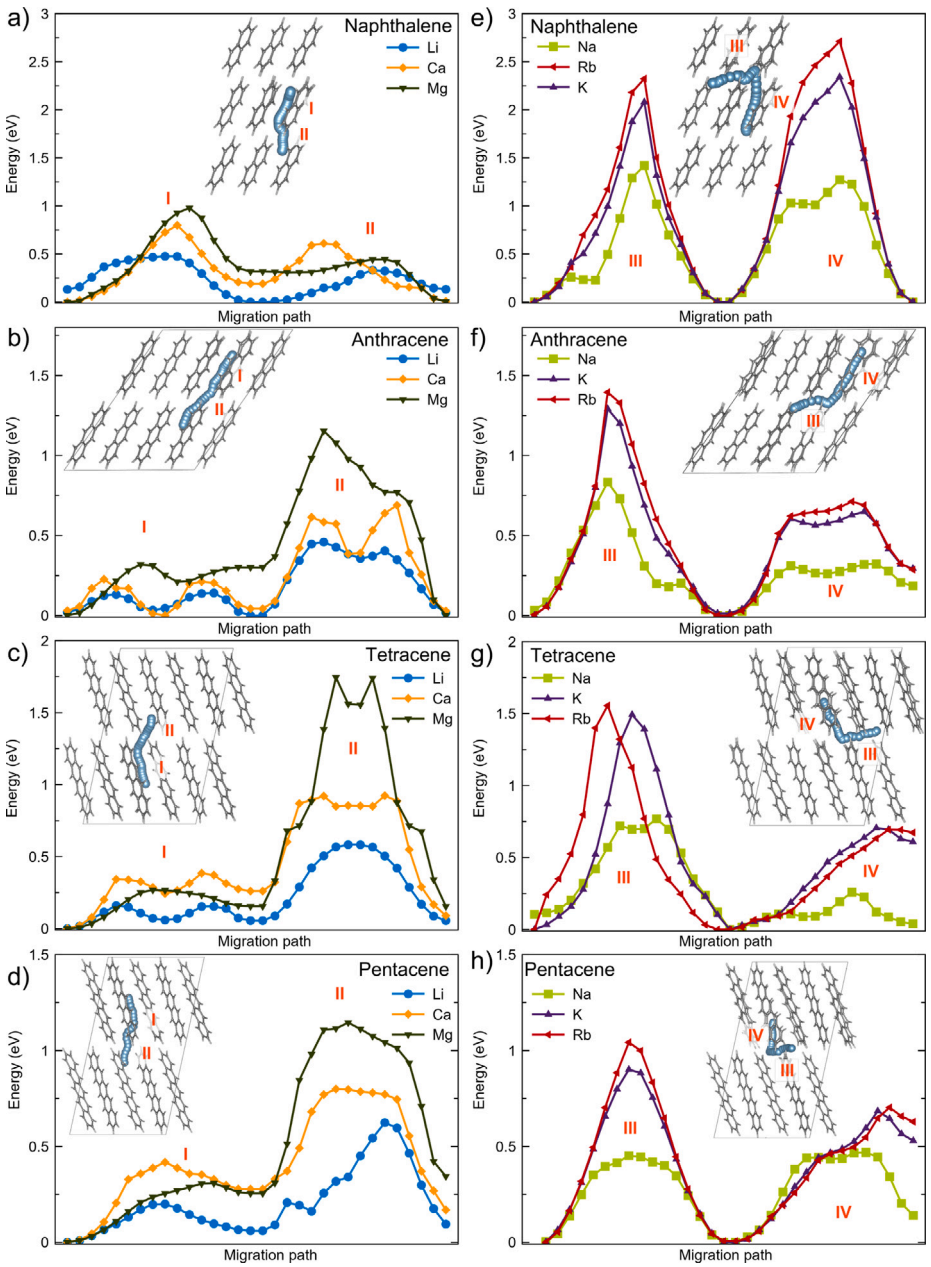

Fig. 6. Migration barrier of metal atoms in (a, e) naphthalene, (b, f) anthracene, (c, g) tetracene and (d, h) pentacene. Simulated migration pathways are shown in the insets.

with Mg, Ca, Li, Na, K, Rb atoms. Only tetracene and pentacene with intercalated Ca, Li, Na, K are dynamically and thermodynamically stable. Intercalation with calcium, lithium, and sodium in pentacene leads to volume changes of 5.2%, 0.8%, and 3.4%, respectively, which indicate the potential for using pentacene crystals in batteries. The capacity of PAH crystals with Li, Na, K and Rb can be ~ 1.2–1.3 times higher than the theoretical capacity of lithium intercalated graphite, while the intercalation of Mg and Ca leads to even higher capacities, which are ~ 2.3–2.6 times higher. Therefore PAH crystals could hypothetically be a more capacious anode material than graphite. For all PAH crystals the diffusion barriers for Li and Ca are low (≤0.6 eV and ≤0.95 eV respectively), while for Na it is ≤0.3 eV. Our results provide insight into the thermodynamics and kinetics of metal intercalation in PAH crystals. Values of binding energy, satisfactory activation barriers of diffusion, low volume changes make PAH crystals (tetracene and pentacene) promising anode materials for Ca, Li, Na-ion batteries.

CRediT authorship contribution statement

Ilya V. Chepkasov: Writing – review & editing, Writing – original draft, Visualization, Investigation, Data curation, Conceptualization. **Viktor S. Baidyshev:** Software, Investigation. **Alexander G. Kvashnin:** Writing – review & editing, Writing – original draft, Visualization, Supervision, Investigation.

Declaration of competing interest

The authors declare that they have no known competing financial interests or personal relationships that could have appeared to influence the work reported in this paper.

Acknowledgment

The authors are grateful to Arkady V. Krasheninnikov (HZDR) and Alexey P. Maltsev (Skoltech) for the discussion. The research was

carried out using resources of the Center for the Information and Computing of Novosibirsk State University.

Appendix A. Supplementary data

Supplementary material related to this article can be found online at https://doi.org/10.1016/j.est.2025.116831.

Data availability

Data will be made available on request.

References

[1] R. Marom, S.F. Amalraj, N. Leifer, D. Jacob, D. Aurbach, A review of advanced and practical lithium battery materials, J. Mater. Chem. 21 (27) (2011) 9938–9954.

[2] G.-A. Nazri, G. Pistoia, Lithium Batteries: Science and Technology, Springer Science & Business Media, 2008.

[3] M. Armand, J.-M. Tarascon, Building better batteries, Nature 451 (7179) (2008) 652–657.

[4] G. Girishkumar, B. McCloskey, A.C. Luntz, S. Swanson, W. Wilcke, Lithium- air battery: promise and challenges, J. Phys. Chem. Lett. 1 (14) (2010) 2193–2203.

[5] T.-H. Kim, J.-S. Park, S.K. Chang, S. Choi, J.H. Ryu, H.-K. Song, The current move of lithium ion batteries towards the next phase, Adv. Energy Mater. 2 (7) (2012) 860–872.

[6] B. Scrosati, J. Garche, Lithium batteries: Status, prospects and future, J. Power Sources 195 (9) (2010) 2419–2430.

[7] R. Wang, L. Wang, R. Liu, X. Li, Y. Wu, F. Ran, "Fast-charging" anode materials for lithium-ion batteries from perspective of ion diffusion in crystal structure, ACS Nano 18 (4) (2024) 2611–2648.

[8] A.V. Iosimovska, A.P. Maltsev, I.V. Chepkasov, A.R. Oganov, Thermodynamic stability and ionic conductivity in lithium–germanium binary system, Appl. Phys. Lett. 124 (16) (2024).

[9] A.P. Maltsev, I.V. Chepkasov, A.G. Kvashnin, A.R. Oganov, Ionic conductivity of lithium phosphides, Crystals 13 (5) (2023) 756.

[10] A.P. Maltsev, I.V. Chepkasov, A.R. Oganov, Order–disorder phase transition and ionic conductivity in a li2b12h12 solid electrolyte, ACS Appl. Mater. & Interfaces 15 (36) (2023) 42511–42519.

[11] H. Cheng, J.G. Shapter, Y. Li, G. Gao, Recent progress of advanced anode materials of lithium-ion batteries, J. Energy Chem. 57 (2021) 451–468.

[12] P. Li, S. Luo, L. Zhang, Q. Liu, Y. Wang, Y. Lin, C. Xu, J. Guo, P. Cheali, X. Xia, Progress, challenges, and prospects of spent lithium-ion batteries recycling: a review, J. Energy Chem. 89 (2024) 144–171.

[13] F. Duffner, N. Kronemeyer, J. Tübke, J. Leker, M. Winter, R. Schmuch, Post-lithium-ion battery cell production and its compatibility with lithium-ion cell production infrastructure, Nat. Energy 6 (2) (2021) 123–134.

[14] J. Fleischmann, M. Hanicke, E. Horetsky, D. Ibrahim, S. Jautelat, M. Linder, P. Schaufuss, L. Torscht, A. van de Rijt, Battery 2030: Resilient, sustainable, and circular, McKinsey & Co. (2023) 2–18.

[15] E. Goikolea, V. Palomares, S. Wang, I.R. de Larramendi, X. Guo, G. Wang, T. Rojo, Na-ion batteries—approaching old and new challenges, Adv. Energy Mater. 10 (44) (2020) 2002055.

[16] A. Zhao, Y. Fang, X. Ai, H. Yang, Y. Cao, Mixed polyanion cathode materials: Toward stable and high-energy sodium-ion batteries, J. Energy Chem. 60 (2021) 635–648.

[17] T. Hosaka, K. Kubota, A.S. Hameed, S. Komaba, Research development on K-ion batteries, Chem. Rev. 120 (14) (2020) 6358–6466.

[18] T. Li, Q. Zhang, Advanced metal sulfide anode for potassium ion batteries, J. Energy Chem. 27 (2) (2018) 373–374.

[19] B. Lu, N. Ru, J. Duan, Z. Li, J. Qu, In-plane porous graphene: A promising anode material with high ion mobility and energy storage for rubidium-ion batteries, ACS Omega 8 (24) (2023) 21842–21852.

[20] J. Niu, Z. Zhang, D. Aurbach, Alloy anode materials for rechargeable Mg ion batteries, Adv. Energy Mater. 10 (23) (2020) 2000697.

[21] X. Chai, H. Xie, T.-T. Zhang, Y. Xin, F. Zhang, B. He, H. Xie, L. Yu, H. Tian, Ternary Mg alloy-based artificial interphase enables high-performance rechargeable magnesium batteries, Energy Storage Mater. (2024) 103460.

[22] T. Masese, G. Kanyolo, Electrode materials for calcium batteries: Future directions and perspectives, 2024.

[23] A. Taghavi-Kahagh, H. Roghani-Mamaqani, M. Salami-Kalajahi, Powering the future: A comprehensive review on calcium-ion batteries, J. Energy Chem. 90 (2024) 77–97.

[24] J. Xu, Y. Dou, Z. Wei, J. Ma, Y. Deng, Y. Li, H. Liu, S. Dou, Recent progress in graphite intercalation compounds for rechargeable metal (Li, Na, K, Al)-ion batteries, Adv. Sci. 4 (10) (2017) 1700146, http://dx.doi.org/10.1002/advs.201700146.

[25] K. Ji, J. Han, A. Hirata, T. Fujita, Y. Shen, S. Ning, P. Liu, H. Kashani, Y. Tian, Y. Ito, J.-i. Fujita, Y. Oyama, Lithium intercalation into bilayer graphene, Nat. Commun. 10 (1) (2019) 275, http://dx.doi.org/10.1038/s41467-018-07942-z.

[26] F.J. Sonia, M.K. Jangid, B. Ananthoju, M. Aslam, P. Johari, A. Mukhopadhyay, Understanding the li-storage in few layers graphene with respect to bulk graphite: experimental, analytical and computational study, J. Mater. Chem. A 5 (18) (2017) 8662–8679, http://dx.doi.org/10.1039/C7TA01978E.

[27] S. Yuan, Q. Lai, X. Duan, Q. Wang, Carbon-based materials as anode materials for lithium-ion batteries and lithium-ion capacitors: A review, J. Energy Storage 61 (2023) 106716.

[28] A.K. Prajapati, A. Bhatnagar, A review on anode materials for lithium/sodium-ion batteries, J. Energy Chem. (2023).

[29] W. Zhao, C. Zhao, H. Wu, L. Li, C. Zhang, Progress, challenge and perspective of graphite-based anode materials for lithium batteries: A review, J. Energy Storage 81 (2024) 110409.

[30] I.V. Chepkasov, M. Ghorbani-Asl, Z.I. Popov, J.H. Smet, A.V. Krasheninnikov, Alkali metals inside bi-layer graphene and MoS2: Insights from first-principles calculations, Nano Energy 75 (2020) 104927, http://dx.doi.org/10.1016/j.nanoen.2020.104927.

[31] M. Kühne, F. Börrnert, S. Fecher, M. Ghorbani-Asl, J. Biskupek, D. Samuelis, A.V. Krasheninnikov, U. Kaiser, J.H. Smet, Reversible superdense ordering of lithium between two graphene sheets, Nature 564 (7735) (2018) 234–239, http://dx.doi.org/10.1038/s41586-018-0754-2.

[32] I.V. Chepkasov, J.H. Smet, A.V. Krasheninnikov, Single-and multilayers of alkali metal atoms inside graphene/mos2 heterostructures: A systematic first-principles study, J. Phys. Chem. C 126 (37) (2022) 15558–15564, http://dx.doi.org/10.1021/acs.jpcc.2c03749.

[33] X. Zhang, M. Ghorbani-Asl, Y. Zhang, A.V. Krasheninnikov, Quasi-2D FCC lithium crystals inside defective bi-layer graphene: insights from first-principles calculations, Mater. Today Energy 34 (2023) 101293.

[34] H. Zhang, Y. Yang, D. Ren, L. Wang, X. He, Graphite as anode materials: Fundamental mechanism, recent progress and advances, Energy Storage Mater. 36 (2021) 147–170.

[35] Z. Zhang, Y. Zhou, P. Chen, S. Zeng, W. Nie, Y. Xu, Investigation of capacity increase in schiff-base networks as the organic anode for lithium-ion batteries, ACS Appl. Energy Mater. 4 (11) (2021) 12882–12891.

[36] H.-g. Wang, S. Yuan, Z. Si, X.-b. Zhang, Multi-ring aromatic carbonyl compounds enabling high capacity and stable performance of sodium-organic batteries, Energy Environ. Sci. 8 (11) (2015) 3160–3165.

[37] L. Tao, J. Zhao, J. Chen, C. Ou, W. Lv, S. Zhong, 1, 4, 5, 8-naphthalenetetracarboxylic dianhydride grafted phthalocyanine macromolecules as an anode material for lithium ion batteries, Nanoscale Adv. 3 (11) (2021) 3199–3215.

[38] J. Park, C.W. Lee, S.H. Joo, J.H. Park, C. Hwang, H.-K. Song, Y.S. Park, S.K. Kwak, S. Ahn, S.J. Kang, Contorted polycyclic aromatic hydrocarbon: promising li insertion organic anode, J. Mater. Chem. A 6 (26) (2018) 12589–12597.

[39] D. Kong, T. Cai, H. Fan, H. Hu, X. Wang, Y. Cui, D. Wang, Y. Wang, H. Hu, M. Wu, et al., Polycyclic aromatic hydrocarbons as a new class of promising cathode materials for aluminum-ion batteries, Angew. Chem. Int. Ed. 61 (3) (2022) e202114681, http://dx.doi.org/10.1002/anie.202114681.

[40] J.H. Park, T. Liu, K.C. Kim, S.W. Lee, S.S. Jang, Systematic molecular design of ketone derivatives of aromatic molecules for lithium-ion batteries: First-principles DFT modeling, ChemSusChem 10 (7) (2017) 1584–1591, http://dx.doi.org/10.1002/cssc.201601730.

[41] P.K. Ramya, C.H. Suresh, Polycyclic aromatic hydrocarbons as anode materials in lithium-ion batteries: A DFT study, J. Phys. Chem. A 127 (11) (2023) 2511–2522, http://dx.doi.org/10.1021/acs.jpca.3c00337.

[42] U. Younis, I. Muhammad, Y. Kawazoe, Q. Sun, Design of tetracene-based metallic 2D carbon materials for Na-and K-ion batteries, Appl. Surf. Sci. 521 (2020) 146456, http://dx.doi.org/10.1016/j.apsusc.2020.146456.

[43] S. Das, S. Manna, B. Pathak, Unlocking the potential of dual-ion batteries: Identifying polycyclic aromatic hydrocarbon cathodes and intercalating salt combinations through machine learning, ACS Appl. Mater. & Interfaces 15 (47) (2023) 54520–54529.

[44] Y.-S. Su, J.-K. Chang, Polycyclic aromatic hydrocarbon-enabled wet chemical prelithiation and presodiation for batteries, Batteries 8 (8) (2022) 99.

[45] S. Das, P. Bhauriyal, B. Pathak, Polycyclic aromatic hydrocarbons as prospective cathodes for aluminum organic batteries, J. Phys. Chem. C 125 (1) (2020) 49–57.

[46] X. Zhu, Y. Yang, X. Shu, T. Xu, Y. Jing, Computational insights into the rational design of organic electrode materials for metal ion batteries, Wiley Interdiscip. Rev.: Comput. Mol. Sci. 13 (5) (2023) e1660.

[47] A.P. Maltsev, I.V. Chepkasov, A.R. Oganov, New promising class of anode materials for Ca-ion battery: polyaromatic hydrocarbons, Mater. Today Energy 39 (2024) 101467.

[48] I.V. Chepkasov, A.V. Krasheninnikov, Tetracene crystals as promising anode material for alkali metal ion batteries, Carbon 213 (2023) 118190.

[49] A.V. Krasheninnikov, Y.-C. Lin, K. Suenaga, Graphene bilayer as a template for manufacturing novel encapsulated 2D materials, Nano Lett. (2024).

[50] Y. Li, F. Börrnert, M. Ghorbani-Asl, J. Biskupek, X. Zhang, Y. Zhang, D. Bresser, A.V. Krasheninnikov, U. Kaiser, In situ TEM investigation of the lithiation and delithiation process between graphene sheets in the presence of atomic defects, Adv. Funct. Mater. (2024) 2406034.

[51] Z. Song, H. Zhou, Towards sustainable and versatile energy storage devices: an overview of organic electrode materials, Energy Environ. Sci. 6 (8) (2013) 2280–2301.

[52] K.C. Kim, Design strategies for promising organic positive electrodes in lithium-ion batteries: quinones and carbon materials, Ind. Eng. Chem. Res. 56 (42) (2017) 12009–12023.

[53] S. Muench, A. Wild, C. Friebe, B. Haupler, T. Janoschka, U.S. Schubert, Polymer-based organic batteries, Chem. Rev. 116 (16) (2016) 9438–9484.

[54] T. Nokami, T. Matsuo, Y. Inatomi, N. Hojo, T. Tsukagoshi, H. Yoshizawa, A. Shimizu, H. Kuramoto, K. Komae, H. Tsuyama, et al., Polymer-bound pyrene-4, 5, 9, 10-tetraone for fast-charge and-discharge lithium-ion batteries with high capacity, J. Am. Chem. Soc. 134 (48) (2012) 19694–19700.

[55] S. Panigrahi, G.N. Sastry, Reducing polyaromatic hydrocarbons: the capability and capacity of lithium, Rsc Adv. 4 (28) (2014) 14557–14563.

[56] D. Vijay, G.N. Sastry, Exploring the size dependence of cyclic and acyclic π-systems on cation–π binding, Phys. Chem. Chem. Phys. 10 (4) (2008) 582–590.

[57] S. Ishikawa, G. Madjarova, T. Yamabe, First-principles study of the lithium interaction with polycyclic aromatic hydrocarbons, J. Phys. Chem. B 105 (48) (2001) 11986–11993.

[58] T.A. Baker, M. Head-Gordon, Modeling the charge transfer between alkali metals and polycyclic aromatic hydrocarbons using electronic structure methods, J. Phys. Chem. A 114 (37) (2010) 10326–10333.

[59] R. Friedlein, X. Crispin, W.R. Salaneck, Molecular parameters controlling the energy storage capability of lithium polyaromatic hydrocarbon intercalation compounds, J. Power Sources 129 (1) (2004) 29–33.

[60] A. Arya, S.-L. Hsu, C.-Y. Liu, M.-Y. Chang, J.-K. Chang, E.Y.-T. Li, Y.-S. Su, Small-molecule polycyclic aromatic hydrocarbons as exceptional long-cycle-life li-ion battery anode materials, Small Struct. (2024) 2400273.

[61] G. Kresse, J. Furthmüller, Efficient iterative schemes for ab initio total-energy calculations using a plane-wave basis set, Phys. Rev. B 54 (16) (1996) 11169, http://dx.doi.org/10.1103/PhysRevB.54.11169.

[62] G. Kresse, D. Joubert, From ultrasoft pseudopotentials to the projector augmented-wave method, Phys. Rev. B 59 (3) (1999) 1758, http://dx.doi.org/10.1103/PhysRevB.59.1758.

[63] G. Kresse, J. Furthmüller, Efficiency of ab-initio total energy calculations for metals and semiconductors using a plane-wave basis set, Comput. Mater. Sci. 6 (1) (1996) 15–50.

[64] J.P. Perdew, K. Burke, M. Ernzerhof, Generalized gradient approximation made simple, Phys. Rev. Lett. 77 (18) (1996) 3865.

[65] H.J. Monkhorst, J.D. Pack, Special points for brillouin-zone integrations, Phys. Rev. B 13 (12) (1976) 5188, http://dx.doi.org/10.1103/PhysRevB.13.5188.

[66] K. Momma, F. Izumi, VESTA: a three-dimensional visualization system for electronic and structural analysis, J. Appl. Crystallogr. 41 (3) (2008) 653–658, http://dx.doi.org/10.1107/S0021889808012016.

[67] G. Henkelman, B.P. Uberuaga, H. Jónsson, A climbing image nudged elastic band method for finding saddle points and minimum energy paths, J. Chem. Phys. 113 (22) (2000) 9901–9904, http://dx.doi.org/10.1063/1.1329672.

[68] M.T. Ruggiero, A. Erba, R. Orlando, T.M. Korter, Origins of contrasting copper coordination geometries in crystalline copper sulfate pentahydrate, Phys. Chem. Chem. Phys. 17 (46) (2015) 31023–31029.

[69] V.L. Deringer, A.L. Tchougréeff, R. Dronskowski, Crystal orbital hamilton population (COHP) analysis as projected from plane-wave basis sets, J. Phys. Chem. A 115 (21) (2011) 5461–5466.

[70] T. Björkman, A. Gulans, A.V. Krasheninnikov, R.M. Nieminen, Van der waals bonding in layered compounds from advanced density-functional first-principles calculations, Phys. Rev. Lett. 108 (23) (2012) 235502.

[71] T. Björkman, A. Gulans, A. Krasheninnikov, R. Nieminen, Are we van der waals ready? J. Phys.: Condens. Matter. 24 (42) (2012) 424218.

[72] S.A. Tawfik, T. Gould, C. Stampfl, M.J. Ford, Evaluation of van der waals density functionals for layered materials, Phys. Rev. Mater. 2 (3) (2018) 034005, http://dx.doi.org/10.1103/PhysRevMaterials.2.034005.

[73] C. Tantardini, F.N. Jalolov, A.G. Kvashnin, Crystal structure evolution of fluorine under high pressure, J. Phys. Chem. C 126 (27) (2022) 11358–11364.

[74] S. Grimme, Semiempirical GGA-type density functional constructed with a long-range dispersion correction, J. Comput. Chem. 27 (15) (2006) 1787–1799, http://dx.doi.org/10.1002/jcc.20495.

[75] S. Grimme, J. Antony, S. Ehrlich, H. Krieg, A consistent and accurate ab initio parametrization of density functional dispersion correction (DFT-D) for the 94 elements H-Pu, J. Chem. Phys. 132 (15) (2010) 154104, http://dx.doi.org/10.1063/1.3382344.

[76] S. Grimme, S. Ehrlich, L. Goerigk, Effect of the damping function in dispersion corrected density functional theory, J. Comput. Chem. 32 (7) (2011) 1456–1465, http://dx.doi.org/10.1002/jcc.21759.

[77] A. Tkatchenko, R.A. DiStasio Jr., R. Car, M. Scheffler, Accurate and efficient method for many-body van der waals interactions, Phys. Rev. Lett. 108 (23) (2012) 236402.

[78] A. Tkatchenko, M. Scheffler, Accurate molecular van der waals interactions from ground-state electron density and free-atom reference data, Phys. Rev. Lett. 102 (7) (2009) 073005, http://dx.doi.org/10.1103/PhysRevLett.102.073005.

[79] S.N. Steinmann, C. Corminboeuf, A generalized-gradient approximation exchange hole model for dispersion coefficients, J. Chem. Phys. 134 (4) (2011) 044117, http://dx.doi.org/10.1063/1.3545985.

[80] T. Gould, S. Lebegue, J.G. Ángyán, T. Bucko, A fractionally ionic approach to polarizability and van der waals many-body dispersion calculations, J. Chem. Theory Comput. 12 (12) (2016) 5920–5930.

[81] M. Dion, H. Rydberg, E. Schröder, D.C. Langreth, B.I. Lundqvist, Van der waals density functional for general geometries, Phys. Rev. Lett. 92 (24) (2004) 246401, http://dx.doi.org/10.1103/PhysRevLett.92.246401.

[82] J. Klimeš, D.R. Bowler, A. Michaelides, Van der waals density functionals applied to solids, Phys. Rev. B 83 (19) (2011) 195131, http://dx.doi.org/10.1103/PhysRevB.83.195131.

[83] J. Klimeš, D.R. Bowler, A. Michaelides, Chemical accuracy for the van der waals density functional, J. Phys.: Condens. Matter. 22 (2) (2009) 022201, http://dx.doi.org/10.1088/0953-8984/22/2/022201.

[84] H. Peng, Z.-H. Yang, J.P. Perdew, J. Sun, Versatile van der waals density functional based on a meta-generalized gradient approximation, Phys. Rev. X 6 (4) (2016) 041005, http://dx.doi.org/10.1103/PhysRevX.6.041005.

[85] T. Bucko, S. Lebegue, J. Hafner, J.G. Angyan, Improved density dependent correction for the description of London dispersion forces, J. Chem. Theory Comput. 9 (10) (2013) 4293–4299, http://dx.doi.org/10.1021/ct400694h.

[86] I. Hamada, Van der waals density functional made accurate, Phys. Rev. B 89 (12) (2014) 121103, http://dx.doi.org/10.1103/PhysRevB.89.121103.

[87] K. Lee, É.D. Murray, L. Kong, B.I. Lundqvist, D.C. Langreth, Higher-accuracy van der waals density functional, Phys. Rev. B 82 (8) (2010) 081101, http://dx.doi.org/10.1103/PhysRevB.82.081101.

[88] J. Park, B.D. Yu, S. Hong, Van der waals density functional theory study for bulk solids with BCC, FCC, and diamond structures, Curr. Appl. Phys. 15 (8) (2015) 885–891, http://dx.doi.org/10.1016/j.cap.2015.03.028.

[89] C. Tantardini, A.R. Oganov, Thermochemical electronegativities of the elements, Nat. Commun. 12 (1) (2021) 2087, http://dx.doi.org/10.1038/s41467-021-22429-0.

[90] Y. Liu, B.V. Merinov, W.A. Goddard, Origin of low sodium capacity in graphite and generally weak substrate binding of Na and Mg among alkali and alkaline earth metals, Proc. Natl. Acad. Sci. 113 (14) (2016) 3735–3739, http://dx.doi.org/10.1073/pnas.1602473113.

[91] H. Moriwake, A. Kuwabara, C.A. Fisher, Y. Ikuhara, Why is sodium-intercalated graphite unstable? RSC Adv. 7 (58) (2017) 36550–36554, http://dx.doi.org/10.1039/C7RA06777A.

[92] C. Hartwigsen, W. Witschel, E. Spohr, Charge density and charge transfer in stage-1 alkali-graphite intercalation compounds, Phys. Rev. B 55 (8) (1997) 4953, http://dx.doi.org/10.1103/PhysRevB.55.4953.

[93] W. Tang, E. Sanville, G. Henkelman, A grid-based bader analysis algorithm without lattice bias, J. Phys.: Condens. Matter. 21 (8) (2009) 084204.

[94] E. Levi, M. Levi, O. Chasid, D. Aurbach, A review on the problems of the solid state ions diffusion in cathodes for rechargeable Mg batteries, J. Electroceramics 22 (2009) 13–19.

[95] M. Walter, M.V. Kovalenko, K.V. Kravchyk, Challenges and benefits of post-lithium-ion batteries, New J. Chem. 44 (5) (2020) 1677–1683.

[96] K. Zhong, R. Hu, G. Xu, Y. Yang, J.-M. Zhang, Z. Huang, Adsorption and ultrafast diffusion of lithium in bilayer graphene: Ab initio and kinetic Monte Carlo simulation study, Phys. Rev. B 99 (15) (2019) 155403, http://dx.doi.org/10.1103/PhysRevB.99.155403.